

Generation of out-of-plane polarized spin current by non-uniform oxygen octahedral tilt/rotation

Received: 7 February 2024

Accepted: 19 August 2024

Published online: 24 August 2024

 Check for updates

Furong Han^{1,7}, Jing Zhang^{2,7}, Fan Yang^{3,7}, Bo Li¹, Yu He¹, Guansong Li⁴, Youxiang Chen¹, Qisheng Jiang², Yan Huang¹, Hui Zhang¹, Jine Zhang¹, Huaiwen Yang¹, Huiying Liu³, Qinghua Zhang⁴, Hao Wu², Jingsheng Chen⁵, Weisheng Zhao¹, Xian-Lei Sheng³✉, Jirong Sun^{4,6}✉ & Yue Zhang¹✉

The free-field switching of the perpendicular magnetization by the out-of-plane polarized spin current induced spin-orbit torque makes it a promising technology for developing high-density memory and logic devices. The materials intrinsically with low symmetry are generally utilized to generate the spin current with out-of-plane spin polarization. However, the generation of the out-of-plane polarized spin current by engineering the symmetry of materials has not yet been reported. Here, we demonstrate that paramagnetic CaRuO₃ films are able to generate out-of-plane polarized spin current by engineering the crystal symmetry. The non-uniform oxygen octahedral tilt/rotation along film's normal direction induced by oxygen octahedral coupling near interface breaks the screw-axis and glide-plane symmetries, which gives rise to a significant out-of-plane polarized spin current. This spin current can drive field-free spin-orbit torque switching of perpendicular magnetization with high efficiency. Our results offer a promising strategy based on crystal symmetry design to manipulate spin current and could have potential applications in advanced spintronic devices.

The spin current originating from the spin Hall effect¹ or Rashba-Edelstein effect² allows one to effectively control the magnetization in ferromagnets through spin-orbit torque (SOT), constituting the basis of energy-economic, high-performance magnetic memory and spin logic^{3–5}. Meanwhile, the polarization direction of spin current is constrained by crystal symmetry and strictly perpendicular to the directions of charge (*x*-direction) and spin flows (*z*-direction) in high-symmetry materials (*y*-direction polarized)^{6,7}. This *y*-direction polarized spin current is only effective for manipulating the samples with in-

plane magnetic anisotropy. Towards high-density memory requirement, deterministic switching of perpendicular magnetization is highly desired. In this case, the assistance of an external in-plane magnetic field is required^{8,9}. In addition to external field, additional design to break the in-plane symmetry is also adopted, such as introducing an exchange bias induced by an antiferromagnet^{10,11}, a stray field from a neighboring ferromagnetic layer¹², or engineering the structure with composition gradient¹³. However, all these make it much more complex to design relevant spintronic devices. One way to

¹Fert Beijing Research Institute, National Key Lab of Spintronics, School of Integrated Circuit Science and Engineering, Beihang University, 100191 Beijing, P. R. China. ²Songshan Lake Materials Laboratory, Dongguan, 523808 Guangdong, P. R. China. ³School of Physics, Beihang University, 100191 Beijing, P. R. China. ⁴Beijing National Laboratory for Condensed Matter Physics & Institute of Physics, Chinese Academy of Sciences, 100190 Beijing, P. R. China. ⁵Department of Materials Science and Engineering, National University of Singapore, Singapore 117575, Singapore. ⁶Spintronics Institute, Jinan University, 250022 Jinan, Shandong, P. R. China. ⁷These authors contributed equally: Furong Han, Jing Zhang, Fan Yang. ✉e-mail: xlsheng@buaa.edu.cn; jrsun@iphy.ac.cn; yz@buaa.edu.cn

overcome this problem is to directly obtain out-of-plane polarized spin current, which can achieve perpendicular magnetization switching deterministically without the requirement of the external in-plane magnetic field. It has been demonstrated that the out-of-plane polarized spin current can be generated in the materials with low crystal/magnetic symmetry. For example, out-of-plane polarized spin current was observed in collinear and non-collinear antiferromagnets with low magnetic symmetry^{14–16}, WTe₂/Py bilayers and CuPt/CoPt bilayers with low crystal symmetry^{17–19}. There is still less report on engineering the crystal symmetry to obtain the out-of-plane polarized spin current.

Perovskite oxides are attractive sources for generating spin current, since they possess strong spin-orbit coupling and provide a good platform for crystal symmetry design. The perovskite oxides with 4d/5d transition metals usually have a high efficiency for charge-spin interconversion. As reported, the SOT efficiencies of the SrIrO₃ films (0.3–1.0)^{20,21} and the SrRuO₃ films (0.03–0.89)^{22–24} are much larger than that of the conventional heavy metals, such as Pt (0.013–0.13)^{25,26}. According to the recent work on the SrRuO₃/SrIrO₃ structure, the magnetization switching efficiency of this structure can be one order of magnitude larger than that of the conventional heavy transition metal systems^{27,28}. However, the SOT generated from perovskite oxides is generally limited to the in-plane direction and cannot be directly applied to the switching of perpendicular magnetization. Fortunately, the crystal structure of perovskite oxides in heterostructures can be artificially designed/engineered. It has been demonstrated that the tilt/rotation of oxygen octahedra relaxed along the out-of-plane direction due to its mismatch and coupling with that of the substrate, resulting in changes in crystal symmetry^{29,30}. This provides a wide space for manipulating the polarization of the spin current via symmetry engineering. Therefore, the paramagnetic metal CaRuO₃ (CRO) with large oxygen octahedral tilt/rotation is expected to obtain the out-of-plane polarized spin current.

Here, we report the generation of the out-of-plane polarized spin current by reduction in the crystal symmetry with precisely engineering the oxygen octahedra of perovskite oxide CRO. The CRO films are epitaxially grown on the cubic LaAlO₃ (LAO) substrate which does not have oxygen octahedral tilt/rotation. The mismatch and coupling of oxygen octahedra near CRO/LAO interface result in the gradual change of octahedral tilt/rotation along the out-of-plane direction. This non-uniform structural modification breaks the screw-axis and glide-plane symmetries of CRO. Theoretical analysis shows that this kind of symmetry breaking is sufficient enough for the generation of an out-of-plane polarized spin current. Indeed, spin current-induced out-of-plane SOT is experimentally detected by the technique of spin-torque ferromagnetic resonance (ST-FMR), and efficient field-free perpendicular magnetization switching is achieved with a low threshold current density.

Results and discussion

Oxygen octahedra engineering

The perovskite oxide CRO with GdFeO₃-typed orthorhombic structure exhibits a large oxygen octahedral tilt/rotation and thus a low symmetry space group (*Pbnm*)³¹. The CRO films with thickness of 14 nm were grown on (001)-oriented LAO single crystalline substrate. The LAO is cubic and the oxygen octahedra rotation of CRO layer at interface is expected to follow that of LAO^{29,30}. As well known, bulk CRO possesses the lattice parameters $a = 5.36 \text{ \AA}$, $b = 5.53 \text{ \AA}$ and $c = 7.66 \text{ \AA}$, which can also be represented by a pseudo-cubic structure with $a_{pc} \approx 3.85 \text{ \AA}$. The lattice mismatch between bulk CRO and LAO substrate is -1.53% (“-” denotes compressive strains in CRO). The compressive strains in CRO will affect the degree of the tilt/rotation of the RuO₆ octahedra. The quality of heterostructure was confirmed by scanning transmission electron microscopy (STEM). Fig. 1a shows the high-angle annular dark-field (HAADF) image of the cross section of the

CRO films grown on LAO substrate. The bright and faint dots in the CRO films correspond to Ru and Ca atoms, respectively. The CRO/LAO interface is sharp without interlayer diffusion. Fig. 1b displays the atomic-resolution angular bright field (ABF) image of the CRO films near LAO substrate, from which, the oxygen positions can be easily determined. The colored diagrams depict the tilted oxygen octahedra. The averaged Ru-O-Ru bond angle ϕ as a function of the atomic layer is plotted in left plot of Fig. 1c. The atomic layer neighboring the substrate was defined as the 1st layer of CRO. As expected, the Al-O-Al bond angle of the LAO substrate is approximately 180°, without oxygen octahedral tilt/rotation. For the CRO films, the Ru-O-Ru bond angle is nearly 180° in the atomic layer closest to LAO substrate. Away from the interface, however, the Ru-O-Ru bond angle in the atomic layer relaxes gradually and finally gets a value of $\sim 162^\circ$. The relaxation length scale for the oxygen octahedral tilt/rotation is about 18 unit cells. The displacement x_O of the O anion along the [001]-axis direction, a consequence of octahedral tilt/rotation, is determined quantitatively, and the corresponding results are shown in the right panel of Fig. 1c. The x_O illustrates a gradual increase as the CRO layer shifts away from the CRO/LAO interface, responding the changes of the Ru-O-Ru bond angle. The relaxation of oxygen octahedral tilt/rotation along out-of-plane direction are consistent with reported results^{30,32}. These observations suggest that a non-uniform structural modification along [001]-axis direction takes place in the CRO films though the octahedral structure remains^{33,34}, which is induced by the interfacial oxygen octahedral mismatch and coupling. The gradual change of octahedral tilt/rotation along the out-of-plane direction has been observed in CRO grown on orthorhombic NdGaO₃ substrate, which can be attributed to the regulation of tensile strain and growth conditions³⁵. By designing symmetry mismatched interface in CRO/LAO heterostructure, the gradual change of octahedral tilt/rotation with larger thickness is obtained, in which the trend of gradual change is opposite to that in CRO/NdGaO₃ heterostructure. Fig. 1d shows the $\theta - 2\theta$ x-ray diffraction (XRD) spectra for CRO films with thickness of 14 nm, a main peak and a broad peak (marked by black arrow) are observed, corresponding to LAO substrate and CRO films, respectively. The low surface roughness derived from atomic force microscope (AFM) image and the narrow peak of the rocking curve further confirm that the CRO films have good crystallinity³⁶ (refer to Section 1 of Supplementary Information). The reciprocal space mappings (RSMs) for the (103) reflections of CRO films grown on LAO are shown in Section 2 of Supplementary Information, the reflections of the CRO films are aligning vertically with that of the substrate, which indicates the CRO films are fully coherently grown on the substrate, sharing the same in-plane lattice constant with LAO substrate. Phi scan of the CRO films yields four diffraction peaks with essentially the same positions, demonstrating that the (103) reflection is fourfold symmetric. We further study the anisotropy between the [110] and $[\bar{1}\bar{1}0]$ -axes by resistivity measurements. The differences of resistivity between the two axes are pretty small which confirms the isotropic behavior between the [110] and $[\bar{1}\bar{1}0]$ -axes (refer to Section 3 of Supplementary Information).

Theoretical analysis

Due to the structural modification, the crystal symmetry of the CRO films needs further analyses. The space group of bulk CRO is *Pbnm*, which preserves the inversion *P*, three screw axes $\widetilde{C}_{2a} = \{C_{2a}|T_{1/2,1/2,0}\}$, $\widetilde{C}_{2b} = \{C_{2b}|T_{1/2,1/2,1/2}\}$, $\widetilde{C}_{2c} = \{C_{2c}|T_{0,0,1/2}\}$, two glide plane $\widetilde{M}_a = \{M_a|T_{1/2,1/2,0}\}$, $\widetilde{M}_b = \{M_b|T_{1/2,1/2,1/2}\}$, and mirror $\widetilde{M}_c = \{M_c|T_{0,0,1/2}\}$, where $T_{a,b,c}$ is the translation operator, *a*, *b* and *c* are the axes of the orthorhombic structure. These symmetries will produce constraints on the polarization direction of spin current. When we apply a charge current along the *a*-axis, we can find that the *y*-direction polarized spin

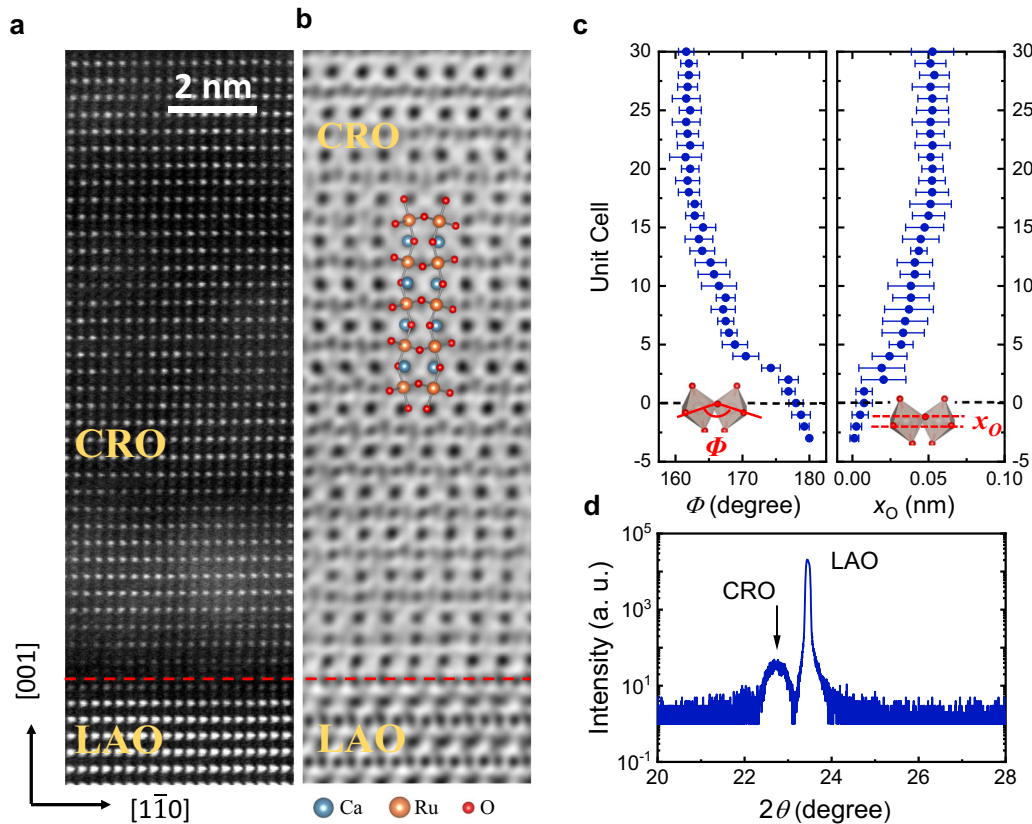


Fig. 1 | Crystal structure of CRO films grown on LAO substrate. **a** HAADF image of the cross-section of CRO (14 nm)/LAO, recorded along the [110] zone axis. The interfaces are marked by red dashed line, showing clearly layered structures and atomically sharp interface. **b** ABF image of CRO (14 nm)/LAO, the interface is marked by red dashed line. The colored diagrams depict the tilted octahedra. **c** Averaged Ru-O-Ru bond angle Φ (left) and displacements of O anion x_O (right)

plotted as a function of the pseudo-cubic CRO layer. The error bars denote the standard deviation of multiple measurements. The Ru-O-Ru band angle Φ and the displacements of O anion x_O are sketched in the inset plots. **d** XRD spectra of the CRO films with the thickness of 14 nm. The black arrow marks the (001) diffraction peak of CRO layers.

current is allowed, but the out-of-plane polarized spin current is forbidden due to the constraint of \widetilde{C}_{2b} , \widetilde{C}_{2c} , \widetilde{M}_b , \widetilde{M}_c (refer to Section 4 of Supplementary Information for the detailed proof). Therefore, the generation of out-of-plane polarized spin current needs symmetry breaking. Fig. 2a schematically shows the relaxation of oxygen octahedral tilt/rotation along out-of-plane direction derived from structural analyses, where a , b and c -axes correspond to the $[1\bar{1}0]$, $[110]$ - and $[001]$ -axes directions of pseudo-cubic structure, respectively. The mirror \widetilde{M}_c cannot be preserved due to the non-uniform structural distortion along the $[001]$ -axis direction, as shown in Fig. 2a. The screw axis \widetilde{C}_{2c} is composed of rotation symmetry C_2 and translation symmetry $T_{0,0,1/2}$ along the c -axis (Fig. 2b), which entails rotating 180° and then translating half a cell of orthorhombic structure along the c -axis. The blue boxes with solid and dashed line mark the locations before and after symmetry operation, respectively. Due to the non-uniform structural distortion along the $[001]$ -axis direction, the translation symmetry $T_{0,0,1/2}$ will not be preserved, thus the screw axis \widetilde{C}_{2c} is broken. Similar to the \widetilde{C}_{2c} , \widetilde{M}_b is also broken, which include the translation operation along c -axis. The \widetilde{C}_{2b} and \widetilde{C}_{2a} cannot be preserved under the structural distortion. However, the glide plane \widetilde{M}_a is preserved, because it only involves the in-plane translation $T_{1/2,1/2,0}$ (refer to Section 5 of Supplementary Information). Based on the above analysis, the CRO with the reduced symmetry could allow out-of-plane polarized spin current when the charge current is applied along the a -axis.

To gain further knowledge about the polarization of the spin current under symmetry breaking, we calculated the intrinsic spin Hall conductivity (SHC) of CRO with non-uniform structural modification using density functional theory (DFT) calculations. To simulate the non-uniform structural modification along the c -axis, we propose a model for CRO as plotted in Fig. 2c. In a single CRO layer, the O anions migrate either upwards or downwards along the c -axis direction represented by green and blue arrows, respectively. Accordingly, the Ru-O-Ru bond angle is altered and exhibits non-uniformity between CRO layers along the c -axis direction, which is consistent with crystal structural analyses. The DFT model of CRO with non-uniform structural modification adopted the same lattice parameters experimentally determined. The surface states from DFT calculations qualitatively match the experimental results³⁷ (refer to Section 6 of Supplementary Information). The corresponding band structure is shown in Fig. 2d, and we project the energy state onto the d_{yz} , d_{xz} and $d_{x^2-y^2}$ orbitals of the Ru ions. It can be seen that the metallic bands near the Fermi energy are mainly formed by these three orbitals. And the three orbitals are hardly involved with deep energy bands. So, we take the d orbitals of the Ru anions to construct the Wannier functions. The SHC element $\sigma_{\alpha\beta\gamma}$ of CRO as a function of energy is demonstrated in Fig. 2e, where, α denotes the direction of the spin flows, β denotes the direction of the applied electric field, and γ denotes the direction of the spin polarization. Here, the external electric field is along the a -axis, and the generated spin current will inject into ferromagnetic layers and induce the SOT. The calculation results show that the $\sigma_{zx,y}$ of y -direction polarized spin current is $(\hbar/2e)1.39 \times 10^4 \Omega^{-1} \text{m}^{-1}$ near the Fermi surface.

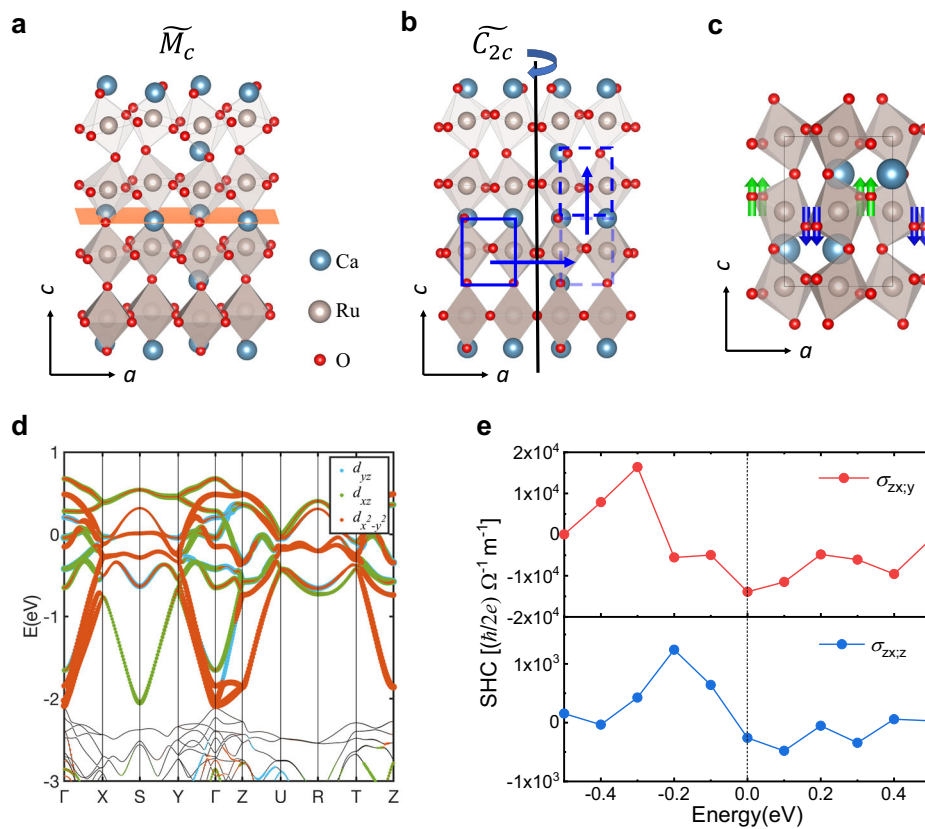


Fig. 2 | Theoretical analysis. **a** Relaxation of oxygen octahedral tilt/rotation along out-of-plane and schematic of mirror \widetilde{M}_c symmetry. The non-uniform oxygen octahedral tilt/rotation introduces difference on either side of the mirror plane and so breaks the mirror symmetry. **b** Schematic of screw axis \widetilde{C}_{2c} . The blue boxes with solid and dashed line mark the location before and after screw axis \widetilde{C}_{2c} operation. **c** Model of CRO with non-uniform structural modification. In a single CRO layer, the

O anions migrate either upwards or downwards along the c -axis direction represented by green and blue arrows, respectively. **d** Electron energy band structures of bulk CRO with distortion. The figure shows the band structure projected onto d_{yz} , d_{xz} and $d_{x^2-y^2}$ orbitals. **e** Spin Hall conductivity of CRO structure with distortion versus the Fermi energy.

As expected, the out-of-plane polarized spin current emerges and $\sigma_{zx,z}$ is $(\hbar/2e)2.59 \times 10^2 \Omega^{-1} \text{m}^{-1}$. For comparison, we calculated the SHC of bulk CRO without lattice distortion, and obtained the result of $\sigma_{zx,z} \approx 0$ (refer to Section 7 of Supplementary Information). The calculation results confirm that CRO with reduced crystal symmetry can generate out-of-plane polarized spin current.

Experimental determination of out-of-plane polarized spin current

The current-induced SOT is evaluated by the technique of ST-FMR, with all the measurements performed at room temperature. For the ST-FMR measurements, the Py (NiFe, 6 nm)/CRO (10 nm) heterostructure were fabricated into a strip with a length of 30 μm and width of 20 μm along the $[1\bar{1}0]$ -axis. The sketch of the ST-FMR measurements is shown in Fig. 3a. A radio frequency current J_c with a frequency of 5 GHz and a power of 15 dBm is applied to the device, which induces an alternating spin current J_s due to the spin Hall effect. The spin current then flows into the adjacent Py layers and exerts a torque on the magnetization. The ST-FMR spectra of Py/CRO device on LAO substrate are shown in Fig. 3b when an in-plane magnetic field with a fixed angle of $\varphi = -45^\circ$ relative to the current axis is applied. The measured voltage signals (V_{mix}) are a superposition of symmetric (V_S) and antisymmetric (V_A) components and can be well described by a Lorentzian function $V_{\text{mix}}(H) = V_A \frac{\Delta(H-H_0)}{(H-H_0)^2 + \Delta^2} + V_S \frac{\Delta^2}{(H-H_0)^2 + \Delta^2}$, where Δ is the linewidth (full width at half maximum) and H_0 is the resonant magnetic field³⁸. Based on the analysis of $V_{\text{mix}}(H)$, the V_S and V_A

components of the spectrum can be determined, and the results are shown in Fig. 3b.

To get further information on SOT, we recorded the ST-FMR spectrum by applying a microwave current with a fixed frequency and sweeping the angle φ from -90° to 270° at a step of 10° , where φ is the angle of the in-plane magnetic field with respect to the direction of the current flow. Different from the case of ordinary heavy metals, the symmetric component V_S and the antisymmetric component V_A of the Py/CRO device cannot be fitted using the conventional torque terms $\cos\varphi\sin 2\varphi$ (τ_y^{DL} and τ_y^{FL} components). They are well described by Eqs. (1) and (2), and the x -, y - and z -direction torque can be separated from the φ dependence voltage signals³⁹

$$V_S(\varphi) \propto \sin 2\varphi[\tau_x^{DL} \sin \varphi + \tau_y^{DL} \cos \varphi + \tau_z^{FL}] \quad (1)$$

$$V_A(\varphi) \propto \sin 2\varphi[\tau_x^{FL} \sin \varphi + \tau_y^{FL} \cos \varphi + \tau_z^{DL}] \quad (2)$$

where τ_x^{DL} , τ_y^{DL} , τ_z^{DL} are coefficients of the damping-like torque generated by the spin Hall effect, and τ_x^{FL} , τ_y^{FL} , τ_z^{FL} are field-like torque counterparts (x , y and z represent the direction of torque). The angular dependences of V_S and V_A of Py/CRO device are respectively shown in Fig. 3c and d, which can be nicely fitted by the Eqs. (1) and (2). The angular dependences of spectra display that V_S is significantly larger than V_A , representing a large damping-like torque efficiency. It can be found that the τ_y^{DL} dominates the V_S signals and the τ_x^{DL} , τ_z^{FL} contribute

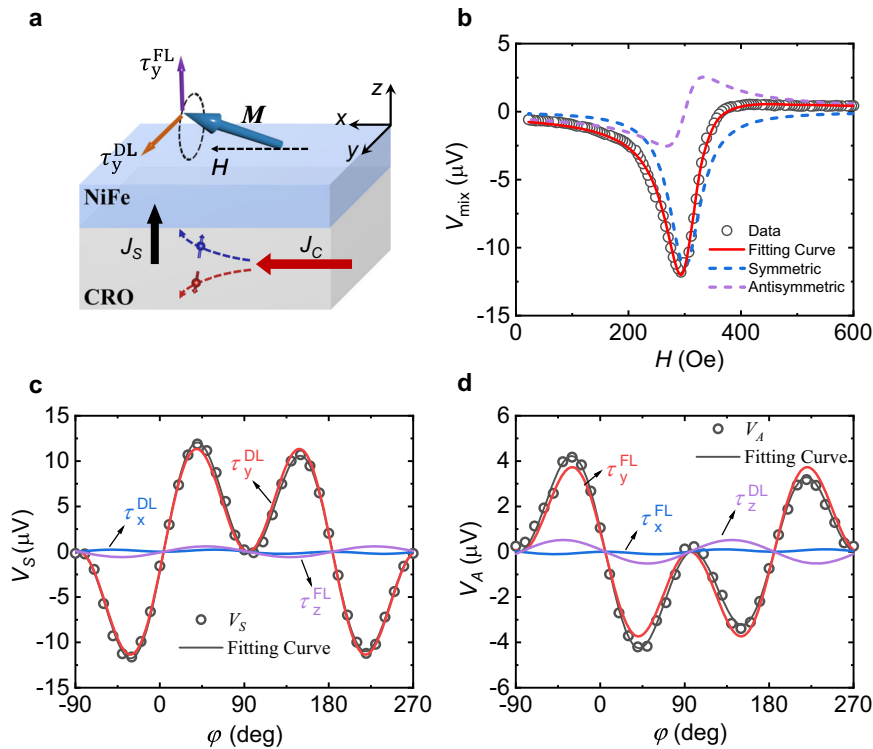


Fig. 3 | ST-FMR measurement. **a** Schematic of ST-FMR measurement. A radio frequency charge current J_C with a frequency of 5 GHz and power of 15 dBm is applied to the device, which induces an alternating spin current J_S due to the spin Hall effect. The spin current then flows into the adjacent Py layer and exerts a torque on the magnetization. The mixing voltage is measured by using lock-in amplifier. **b** ST-FMR spectra of the Py/CRO device at 300 K. The external magnetic field is oriented at $\varphi = -45^\circ$ with respect to the charge current direction. Black

circles denote the measured raw data. Red solid lines are the fitting curves, which are composed of the symmetric (blue short dashed) and antisymmetric (purple short dashed) components. **c, d** Symmetric and antisymmetric voltage amplitudes depending on applied field angle for Py/CRO device. Black circles indicate the extracted values from ST-FMR measurement. The red, blue, and purple curves represent the calculations of τ_x , τ_y , and τ_z , respectively, from the analyses using Eqs. (1) and (2).

a small portion to V_S . The V_A signals are dominated by τ_y^{FL} , which is induced by the Oersted field. The unconventional damping-like torque τ_z^{DL} contributes to V_A signals and cannot be ignored. This result indicates the generation of tilt damping-like torque which does not exist in transition metal oxides with high symmetry. Since the x -direction damping-like torque is forbidden by crystal symmetry, we mainly focus on the y - and z -direction damping-like torque.

From the measurement results, the y - and z -direction damping-like torque efficiencies of CRO films can be evaluated. In ST-FMR, we can use the value of τ_y^{FL} as a measure of the current density in the CRO, allowing us to quantify the amplitude of the damping-like torque efficiencies θ^{DL} per unit current density in CRO:

$$\theta_y^{DL} = \frac{\tau_y^{DL} e \mu_0 M_s t_{Py} t_{CRO}}{\tau_y^{FL} h} \sqrt{1 + \frac{4\pi M_{eff}}{\mu_0 H_0}} \quad (3)$$

$$\theta_z^{DL} = \frac{\tau_z^{DL} e \mu_0 M_s t_{Py} t_{CRO}}{\tau_y^{FL} h} \quad (4)$$

where $4\pi M_{eff}$ is the effective magnetization, $\mu_0 M_s$ is the saturation magnetization, t_{Py} and t_{CRO} are the layer thicknesses of Py and CRO, respectively. By performing ST-FMR with a sequence of microwave frequencies and fitting the resonance fields to the Kittel equation: $f = (\gamma/2\pi) [H_0(H_0 + 4\pi M_{eff})]^{1/2}$, the effective magnetization can be determined, where γ is the gyromagnetic ratio⁴⁰. The effective magnetization of Py/CRO bilayers is 9.81 kOe, as shown in Section 8 of Supplementary Information. The Gilbert damping coefficient α is derived from the linear fitting of line width Δ versus resonant

frequency f : $\Delta = \Delta_0 + (2\pi\alpha/\gamma) f$, and the slope defines the Gilbert damping coefficient, where Δ_0 is the extrinsic contribution that is usually frequency independent⁴¹, and α is 0.010 for Py/CRO bilayers (refer to Section 8 of Supplementary Information). Notably, $\alpha = 0.010$ agrees with the result of the Py films in spin valves⁴¹. The average y -direction torque efficiency θ_y^{DL} of several Py/CRO devices is 1.4. In order to eliminate the influence of resistivity, the magnitude of SHC is provided by a function of $\sigma_y^{DL} = (\hbar/2e)\theta_y^{DL}/\rho_{xx}$. The CRO films exhibit metal conductivity (refer to Section 9 of Supplementary Information). The corresponding σ_y^{DL} reaches $(\hbar/2e)7.7 \times 10^4 \Omega^{-1} \text{m}^{-1}$. The efficiencies of z -direction torque are determined to be 0.0086 and the corresponding σ_z^{DL} is approximately $(\hbar/2e)4.8 \times 10^2 \Omega^{-1} \text{m}^{-1}$, which is on the same order of magnitude as the SHC derived from theoretical calculation.

To exclude Joule heating effect from microwave power, the microwave-power-dependent ST-FMR signals in the CRO/Py device are measured. As the power increases, the voltage of the symmetric component V_S in our device varies linearly, which eliminates the influence of the thermal effect induced by microwave power (refer to Section 10 of Supplementary Information)⁴¹. We further employ second harmonic measurements which can separate the voltages from spin current and Joule heating. The efficiency obtained from second harmonic measurements is 1.2, thus, we conclude that the SOT from spin Hall effect in CRO is predominant, and the contribution of Joule heating is pretty small (refer to Section 10 of Supplementary Information). By comparing the parameters (i.e. effective magnetic field from second harmonic measurement and SOT efficiency from ST-FMR measurement) in a series of $4d/5d$ transition oxides, we can see that the CRO films provide one of the largest efficiencies of charge-spin

interconversion among $4d/5d$ transition oxides (refer to Section 11 of Supplementary Information).

Considering that ferromagnetism can lead to spin currents with out-of-plane polarization, we further analyze the magnetism of CRO films. The results illustrate that the curve of magnetization versus temperature ($M-T$) measured under zero-field-cooled (ZFC) condition coincides very well with the curve under field-cooled (FC) condition. In addition, the curves of magnetization versus field ($M-H$) exhibit almost linear field dependence from 50 K to 300 K, suggesting that CRO films are paramagnetic. At a temperature of 10 K, the $M-H$ curve shows a slightly curvature under lower magnetic fields, implying the existence of possible magnetic order at low temperatures (refer to Section 12 of Supplementary Information)^{42,43}. Due to the fact that both ST-FMR and switching measurements are performed at room temperature, it can be excluded that out-of-plane polarized spin currents originate from ferromagnetism.

The oxygen octahedral tilt/rotation tend to keep uniform for CRO layers near the Py/CRO interface according to the structure analyses. When the thickness of CRO films is increased to 25 nm, the ST-FMR signal is mainly from the CRO layers near Py/CRO interface. The measurements result show that the antisymmetric component V_A can be well fitted simply using the conventional torque terms $\cos\phi\sin 2\phi$, which means that the z -direction SOT can be ignored (refer to Section 13 of Supplementary Information). This result indicates that the Py/CRO interface is different from the Py/WTe₂ interface where the z -direction SOT was observed¹⁷. This difference can be ascribed to the different structural symmetries of CRO and WTe₂: bulk CRO is more symmetric compared to WTe₂. The oxygen octahedral tilt/rotation keeps uniform in CRO layers near the Py/CRO interface, and CRO layers still maintain high symmetry. Thus, the generation of z -direction SOT is forbidden. This result further confirms that the relaxation of oxygen octahedral tilt/rotation near CRO/LAO interface is necessary for the generation of out-of-plane polarized spin current.

In addition, we investigated the in-plane anisotropy of the out-of-plane polarized spin current generated SOT by rotating the ST-FMR measurements device at 90° (refer to Section 14 of the Supplementary Information). According to theoretical analysis, z -direction SOT is forbidden when the charge current is applied along b -axis. However, the z -direction SOT can be observed when the charge current is applied along $[110]$ or $[\bar{1}\bar{1}0]$ -axes, which is consistent with the fourfold symmetry of the CRO films. Due to the twinned crystal domains, both the a -axis and b -axis of orthorhombic structure will grow along the $[110]$ -axis of cubic substrate, destroying the anisotropy between $[110]$ - and $[\bar{1}\bar{1}0]$ -axes^{44–46}. The twinned crystal domains of orthogonal structures produced on a cubic substrate flatten the in-plane anisotropy of SOT in measurement, even though it exists intrinsically.

Numerous studies exhibit that the relaxation of oxygen octahedral tilt/rotation can be controlled by the strain induced from substrate. We further study the z -direction SOT of CRO films under different strain (refer to Section 15 of Supplementary Information). The mismatch between bulk CRO and substrate varies from -1.53% on LAO, $+0.47\%$ on $(\text{LaAlO}_3)_{0.3}(\text{SrAl}_{0.5}\text{Ta}_{0.5}\text{O}_3)_{0.7}$ (LSAT) to $+1.41\%$ on SrTiO₃ (STO) (“ $-$ ” denotes compressive strain, “ $+$ ” denotes tensile strain). The oxygen octahedral tilt/rotation of CRO films grown on STO substrate is derived from STEM image as shown in Fig. S13. The oxygen positions can be easily determined in the atomic-resolution ABF image of the CRO films near STO substrate, as shown in Fig. S13b. The averaged Ru-O-Ru bond angle ϕ as a function of the atomic layer is plotted in left plot of Fig. S13c. As expected, the bond angle of the STO substrate is approximately 180°, without oxygen octahedral tilt/rotation. For the CRO films, the Ru-O-Ru bond angle is nearly 180° in the atomic layer closest to STO substrate. Away from the interface, the Ru-O-Ru bond angle in the atomic layer relaxes gradually and finally gets a value of -176° . The relaxation length scale of the oxygen octahedral tilt/rotation is about 8 unit cells. The displacement x_{O} of the O anion along

the $[001]$ -axis direction gradually increases and saturates as the CRO layer shifts away from the CRO/STO interface as exhibited in the right panel of Fig. S13c. Compared to the CRO films on the LAO substrate, the oxygen octahedral tilt/rotation of CRO films on the STO substrate is suppressed by the tensile strain and the relaxation length scale is reduced, which is consistent with the reported result³⁰. Thus, the thickness of CRO films with non-uniform structural modification is reduced. The SHC of CRO films grown on different substrates is plotted in Fig. S14. The SHC of z -direction polarized spin current demonstrates obvious dependence on the strain, decreasing from compressive strain to tensile strain as shown in Fig. S14d. This trend is consistent with the change of crystal structure under different strains, confirming that the generation of z -direction SOT is dependent on the modification of the structure.

The strain relaxation in cubic or tetragonal materials can result in the gradual change of lattice parameters, which may reduce the crystal symmetry if this material has the symmetries composed of translation operation along the c -axis. However, gradual strain relaxation occurs when the thickness of the films reaches several tens of nanometers, and the amplitude of lattice constant changes is relatively limited. So, it's hard to ensure the generation of obvious z -direction polarized spin current. Compared to the tetragonal or cubic materials, bulk CRO has large oxygen-octahedral rotation/tilt angle. In the absence of strain relaxation, the obvious relaxation of oxygen octahedral in CRO films occurs due to the coupling with substrate, which significantly regulates the Ru-O bond hybridization. Besides the satisfactory of symmetry constraints, large spin Hall effect requires that the material should have strong spin-orbit coupling effect and adequate density of states near the Fermi surface, which is shown in CRO films from our DFT calculations. The above points enhance the perpendicular spin current polarization in CRO films.

Efficient field-free perpendicular magnetization switching

Further investigates demonstrate that the CRO films can provide SOTs that switch of perpendicular magnetization at room temperature without the help of an external magnetic field, favoring high-density spintronic devices. We studied the field-free perpendicular magnetization switching using the out-of-plane polarized spin current from CRO films. For the experiment, we prepared the Ta (2 nm)/MgO (2 nm)/CoFeB (Co₂₀Fe₆₀B₂₀, 1.2 nm)/Ti (3 nm)/CRO (9 nm) multilayer structure, where the Ta and MgO layers were deposited to prevent oxidation of films. The Ti layer is introduced to get perpendicularly magnetized CoFeB layers, and the contribution of current-induced torque from the Ti layer is negligible due to the extremely small spin Hall angle of Ti⁴⁷. The multilayers are fabricated into 16- μm -width Hall bar device and the Ta/MgO/CoFeB/Ti layers are etched into round pillar structure with a diameter of 10 μm (Fig. 4a). The anomalous Hall loops are illustrated in Section 16 of Supplementary Information, which confirm the perpendicular magnetic anisotropy (PMA) of the CoFeB layer. Then we applied a pulsed currents and measured the Hall resistance change for Hall bars. The magnetization can be reversibly switched without external magnetic field H_{ex} as shown in Fig. 4b. $R_{\text{H}}-I_{\text{CRO}}$ loops are obtained under an external magnetic field H_{ex} between $+40$ Oe to -20 Oe along current direction, where R_{H} and I_{CRO} are Hall resistance and the amplitude of the current pulses, respectively. The polarities of the switching loops are opposite when the magnetic field is $+40$ Oe and -20 Oe. Switching of magnetization cannot be achieved with $H_{\text{ex}} = +20$ Oe, which happens when the external magnetic field is equal to the effective internal field. These results confirm that spin current generated from CRO films possesses out-of-plane component which participates in the switching process as effective internal field. The critical current for the field-free switching is 9 mA and the critical current density is as low as $6.3 \times 10^{10} \text{ Am}^{-2}$, which is almost one order of magnitude lower than that of heavy-metal SOT source systems. The comparison with other field-free systems exhibits

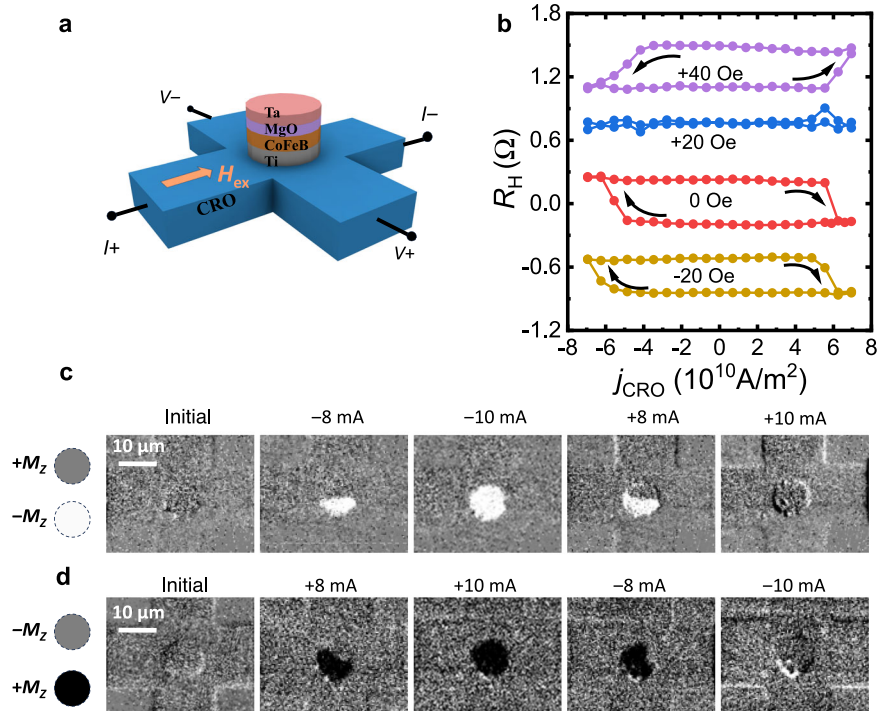


Fig. 4 | Current-induced field-free perpendicular magnetization switching.

a Schematic of the Ta/MgO/CoFeB/Ti/CRO Hall bar device for switching measurements and the Ta/MgO/CoFeB/Ti films are etched into pillar with a diameter of 10 μm. **b** Current-induced magnetization switching of Hall bars device when different in-plane magnetic fields are applied along the direction of the current. The loops are shifted for better visualization and the baseline resistance is about 1.6 Ω. **c, d** Background-subtracted MOKE images of the Hall bar device during field-free SOT switching. To enhance the contrast, the background in the whole image is subtracted, thus, the whole image in the initial state maintains the same color (gray)

though the pillar area is in magnetic polarity state. **c** MOKE images of the field-free SOT switching magnetization from $+M_z$ state to $-M_z$ state. The positive magnetic field was applied along the $+z$ direction to initialize the magnetization to $+M_z$ state. The gray-colored pillar region represents the $+M_z$ state and white-colored pillar region represents the $-M_z$ state. **d** MOKE images of the field-free SOT switching magnetization from $-M_z$ state to $+M_z$ state. The negative magnetic field was applied along the $-z$ direction to initialize the magnetization to $-M_z$. The gray-colored pillar region represents the $-M_z$ state and white-colored pillar region represents the $+M_z$ state.

the high switching efficiency and the advantage of working at room temperature for CoFeB/CRO system (refer to Section 17 of Supplementary Information). When considering the shunting effect, about seventy percent portion of the current flows into the CRO films, and the critical switching current density correspondingly becomes smaller (refer to Section 18 of Supplementary Information). The analysis of Joule heating effect in SOT switching measurement is also performed, from which the CoFeB ferromagnetic layer is found to maintain perpendicularly ferromagnetic even with a rise in temperature (refer to Section 19 of Supplementary Information).

We further verified the switching process by magneto-optical Kerr effect (MOKE) microscopy measurements. Fig. 4c shows the background-subtracted MOKE images of field-free SOT switching magnetization from $+M_z$ state to $-M_z$ state. We initialize the magnetization of the pillar structure to $+M_z$ state by applying a saturation magnetic field along the $+z$ direction and the initial contrast of image is gray after the background is subtracted. Then the external field is set back to zero, when a -8 mA pulsed current is applied into the channel, the pillar area turns white partially, indicating that the magnetization has changed from the $+M_z$ state to the $-M_z$ state partially. When the pulsed current is increased to -10 mA, the pillar area turns white totally, indicating that the magnetization has changed from the $+M_z$ state to the $-M_z$ state totally. After the application of the electric pulse of $+10$ mA, the pillar area turns back to grey, i.e. the magnetization turns back to the $+M_z$ state. In order to confirm the process of magnetization switching, we initialize the magnetic moment to the $-M_z$ state and the contrast is gray after the background is subtracted, as shown in Fig. 4d. The device takes the $+M_z$ state after the electric pulse

of $+10$ mA, then turns back to the $-M_z$ state after the electric pulse of -10 mA (Fig. 4d). Notably, this process is reversible. These results provide direct evidences for the field-free electric switching of the direction of the perpendicular magnetization of CoFeB, driven by the SOT of the CRO films.

In summary, our work demonstrates an approach for generating out-of-plane polarized spin currents in perovskite oxide CRO films. Experimental results and theoretical calculations confirm that the relaxation of oxygen octahedra along out-of-plane direction can serve as an effective way to lower the crystal symmetry, yielding out-of-plane polarized spin current. Efficient field-free perpendicular magnetization switching is realized at room temperature. The present work suggests that engineering crystal symmetry is a promising pathway towards realizing spintronic devices of high density and energy efficiency.

Methods

Sample preparation

The target of CRO was mixed in stoichiometric composition of the elements, with five percent extra RuO₂ to compensate for the rapid evaporation of Ru atom. CRO films was grown on (001)-oriented LAO single crystalline substrate ($5 \times 5 \times 0.5$ mm³) by pulsed laser deposition. The repetition rate is 2 Hz and the fluence is ~ 2 Jcm⁻² (KrF Excimer laser, wavelength = 248 nm). During the deposition process, the substrate temperature was set to 670 °C and the oxygen pressure was maintained at 30 Pa. After deposition, the samples were cooled to room temperature in an oxygen pressure of 100 Pa. The deposition rate of CRO layers was calibrated by X-ray Reflection.

ST-FMR measurements

The CRO films were transferred to the chamber of magnetron sputtering, and the chamber was vacuumed. Then, the Py layers with the thickness of 6 nm were sputter deposited at Ar pressure of 0.35 Pa with a background pressure $\approx 3 \times 10^{-5}$ Pa at room temperature. The SiO₂ (3 nm) layers were fabricated on the top of the heterostructure in order to prevent oxidation of Py layers. For ST-FMR measurements devices, the heterostructure was patterned into rectangular bars with a length of 30 μ m and width of 20 μ m by optical lithography and ion milling techniques. The magnetron sputtering was employed to form electrodes with Ti (20 nm)/Au (80 nm) bilayers. A radio frequency charge current J_c with a frequency of 5 GHz and a power of 15 dBm is applied to the device, which produces a DC mixing voltage and is detected by a bias tee. Then a fixed-frequency microwave current was applied and an in-plane magnetic field was swept at an angle φ with respect to the current flow direction changed from $\varphi = -90^\circ$ to 270° in steps of 10° .

Magnetization switching measurements

The CRO films was then transferred into a magneto sputtering system to grow Ta (2 nm)/MgO (2 nm)/ Co₂₀Fe₆₀B₂₀ (1.2 nm)/Ti (3 nm) stack, with a vacuum of 0.08 Pa. The Ta and Ti layers were deposited using a direct current (DC) power supply. Other materials were deposited using a radio frequency (RF) power supply. The films were fabricated into Hall bar devices of 16 μ m width and the Ta/MgO/CoFeB/Ti layers are etched into round pillar with a diameter of 10 μ m by optical lithography and ion milling techniques. For SOT switching measurements, current pulses (1 ms width) were applied.

Calculation of spin Hall conductivities

Our density functional theory (DFT) calculations are performed by using the Vienna Ab initio Simulation Package (VASP)⁴⁸, with the Perdew-Burke-Ernzerhof (PBE) functional⁴⁹, in the presence of spin-orbit coupling. We take the d orbitals of Ru ions to construct the Wannier functions, using the Wannier 90 package⁵⁰. The calculations of intrinsic spin Hall conductivities are performed in the Wannier Tools package⁵¹, using the Kubo formula

$$\sigma_{\alpha\beta\gamma}(\omega) = -\frac{e^2}{\hbar} \int_{BZ} \frac{d^3\mathbf{k}}{(2\pi)^3} \Omega_{\alpha\beta\gamma}(\mathbf{k}) \quad (5)$$

$$\Omega_{\alpha\beta\gamma}(\mathbf{k}) = -2\hbar^2 \sum_n f_{n\mathbf{k}} \sum_{n' \neq n} \text{Im} \left[\frac{\langle n\mathbf{k} | j_{\alpha\gamma} | n'\mathbf{k} \rangle \langle n'\mathbf{k} | v_\beta | n\mathbf{k} \rangle}{(E_{n'} - E_n)^2 - (\hbar\omega + i\delta)^2} \right] \quad (6)$$

Here $|n\mathbf{k}\rangle$ is the Bloch wavefunction, E_n is the eigenvalue of the Bloch state. $j_{\alpha\gamma} = \frac{1}{2} \{s_\gamma, v_\alpha\}$ is the spin current operator and v_β is the velocity operator, respectively. The finite lifetime broadening δ is set to be 1.00 meV. The subscription α denotes the direction of the linear response current, β denotes the direction of the applied electric field, and γ denotes the direction of the spin polarization. The k -meshes are $5 \times 5 \times 3$ and $200 \times 200 \times 200$ for the self-consistent calculations and the SHC calculations, respectively. The conductivities are multiplied by $(-\hbar/2e)$ to convert into the $(\hbar/2e) \Omega^{-1} \text{m}^{-1}$ units.

Data availability

The authors declare that data generated in this study are provided in the paper and the Supplementary Information file. Further datasets are available from the corresponding author upon request.

Code availability

The authors declare that code supporting the findings of this study is available within the paper and the Supplementary Information file. Further code is available from the corresponding author upon request.

References

- Sinova, J. et al. Spin Hall effects. *Rev. Mod. Phys.* **87**, 1213–1259 (2015).
- Edelstein, V. M. Spin polarization of conduction electrons induced by electric current in two-dimensional asymmetric electron systems. *Solid. State. Commun.* **73**, 233–235 (1990).
- Guo, Z. et al. Spintronics for energy-efficient computing: an overview and outlook. *Proc. IEEE* **109**, 1398 (2021).
- Baek, Sh. C. et al. Complementary logic operation based on electric-field controlled spin-orbit torques. *Nat. Electron.* **1**, 398–403 (2018).
- Zhang, Z. et al. Magnon scattering modulated by omnidirectional hopfion motion in antiferromagnets for meta-learning. *Sci. Adv.* **9**, 7439 (2023).
- Dyakonov, M. I. & Perel, V. Current-induced spin orientation of electrons in semiconductors. *Phys. Lett. A* **35**, 459 (1971).
- Song, C. et al. Spin-orbit torques: Materials, mechanisms, performances, and potential applications. *Prog. Mater. Sci.* **118**, 100761 (2021).
- Liu, L. et al. Symmetry breaking for current-induced magnetization switching. *Appl. Phys. Rev.* **10**, 021319 (2023).
- Zheng, Z. et al. Effective electrical manipulation of a topological antiferromagnet by orbital torques. *Nat. Commun.* **15**, 745 (2024).
- Oh, Y.-W. et al. Field-free switching of perpendicular magnetization through spin-orbit torque in antiferromagnet/ferromagnet/oxide structures. *Nat. Nanotechnol.* **11**, 878 (2016).
- Fukami, S. et al. Magnetization switching by spin-orbit torque in an antiferromagnet-ferromagnet bilayer system. *Nat. Mater.* **15**, 535 (2016).
- Lau, Y.-C. et al. Spin-orbit torque switching without an external field using interlayer exchange coupling. *Nat. Nanotechnol.* **11**, 758 (2016).
- Zheng, Z. et al. Field-free spin-orbit torque-induced switching of perpendicular magnetization in a ferrimagnetic layer with a vertical composition gradient. *Nat. Commun.* **12**, 4555 (2021).
- Karube, S. et al. Observation of Spin-Splitter Torque in Collinear Antiferromagnetic RuO₂. *Phys. Rev. Lett.* **129**, 137201 (2022).
- Nan, T. et al. Controlling spin current polarization through non-collinear antiferromagnetism. *Nat. Commun.* **11**, 4671 (2020).
- Chen, X. et al. Observation of the antiferromagnetic spin Hall effect. *Nat. Mater.* **20**, 800–804 (2021).
- MacNeill, D. et al. Control of spin-orbit torques through crystal symmetry in WTe₂/ferromagnet bilayers. *Nat. Phys.* **13**, 300–305 (2017).
- Kao, I. H. et al. Deterministic switching of a perpendicularly polarized magnet using unconventional spin-orbit torques in WTe₂. *Nat. Mater.* **21**, 1029–1034 (2022).
- Liu, L. et al. Symmetry-dependent field-free switching of perpendicular magnetization. *Nat. Nanotechnol.* **16**, 277–282 (2021).
- Nan, T. et al. Anisotropic spin-orbit torque generation in epitaxial SrIrO₃ by symmetry design. *Proc. Natl. Acad. Sci. USA* **116**, 16186–16191 (2019).
- Wang, H. et al. Large spin-orbit torque observed in epitaxial SrIrO₃ thin films. *Appl. Phys. Lett.* **114**, 232406 (2019).
- Wei, J. et al. Enhancement of Spin-Orbit Torque by Strain Engineering in SrRuO₃ Films. *Adv. Funct. Mater.* **31**, 21000 (2021).
- Zhou, J. et al. Modulation of Spin-Orbit Torque from SrRuO₃ by Epitaxial-Strain-Induced Octahedral Rotation. *Adv. Mater.* **33**, 2007114 (2021).
- Ou, Y. et al. Exceptionally High, Strongly Temperature Dependent, Spin Hall Conductivity of SrRuO₃. *Nano Lett.* **19**, 3663–3670 (2019).
- Liu, L. et al. Spin-Torque Ferromagnetic Resonance Induced by the Spin Hall Effect. *Phys. Rev. Lett.* **106**, 036601 (2011).
- Ando, K. et al. Electric manipulation of spin relaxation using the spin Hall effect. *Phys. Rev. Lett.* **101**, 036601 (2008).

27. Zheng, D. et al. High-efficiency magnon-mediated magnetization switching in all-oxide heterostructures with perpendicular magnetic anisotropy. *Adv. Mater.* **34**, 2203038 (2022).
28. Liu, L. et al. Current-induced magnetization switching in all-oxide heterostructures. *Nat. Nanotechnol.* **14**, 939–944 (2019).
29. Kan, D. et al. Tuning magnetic anisotropy by interfacially engineering the oxygen coordination environment in a transition metal oxide. *Nat. Mater.* **15**, 432–437 (2016).
30. Mun, J. et al. Extended oxygen octahedral tilt proximity near oxide heterostructures. *Nano Lett.* **23**, 1036–1043 (2023).
31. Shepard, M. et al. Magnetic and transport properties of Na doped SrRuO₃ and CaRuO₃. *J. Appl. Phys.* **79**, 4821–4823 (1996).
32. Rondinelli, J. M., May, S. J. & Freeland, J. W. Control of octahedral connectivity in perovskite oxide heterostructures: an emerging route to multifunctional materials discovery. *Mrs Bull.* **37**, 261–270 (2012).
33. He, Q. et al. Towards 3D mapping of BO₆ octahedron rotations at perovskite heterointerfaces, unit cell by unit cell. *ACS Nano* **9**, 8412–8419 (2015).
34. Borisevich, A. Y. et al. Suppression of octahedral tilts and associated changes in electronic properties at epitaxial oxide heterostructure interfaces. *Phys. Rev. Lett.* **105**, 087204 (2010).
35. Sakoda, M. et al. Enhancement of extraordinary size effect on CaRuO₃ ultrathin films. *Adv. Electron. Mater.* **9**, 2201312 (2023).
36. Nair, H. P. et al. Synthesis science of SrRuO₃ and CaRuO₃ epitaxial films with high residual resistivity ratios. *APL Mater.* **6**, 046101 (2018).
37. Liu, Y. et al. Revealing the hidden heavy Fermi liquid in CaRuO₃. *Phys. Rev. B* **98**, 041110 (2018).
38. Mellnik, A. R. et al. Spin-transfer torque generated by a topological insulator. *Nature* **511**, 449–451 (2014).
39. Fang, D. et al. Spin-orbit-driven ferromagnetic resonance. *Nat. Nanotechnol.* **6**, 413–417 (2011).
40. Nan, T. et al. Comparison of spin-orbit torques and spin pumping across NiFe/Pt and NiFe/Cu/Pt interfaces. *Phys. Rev. B* **91**, 214416 (2015).
41. Yang, H. et al. Giant charge-to-spin conversion efficiency in SrTiO₃-based electron gas interface. *Phys. Rev. Appl.* **12**, 034004 (2019).
42. Koriyama, A. et al. Magnetism of CaRuO₃ crystal. *J. Alloys Compd.* **372**, 58–64 (2004).
43. Chen, Y. B. et al. Microstructure and ferromagnetic property in CaRuO₃ thin films with pseudoheterostructure. *Appl. Phys. Lett.* **96**, 182502 (2010).
44. Ricci, F. et al. Mechanism of single-domain selection in epitaxial CaRuO₃ thin films. *Phys. Rev. B* **65**, 155428 (2002).
45. Herranz, G. et al. Controlled magnetic anisotropy of SrRuO₃ thin films grown on nominally exact SrTiO₃(001) substrates. *Appl. Phys. Lett.* **89**, 152501 (2006).
46. Jiang, J. et al. Domain structure of epitaxial SrRuO₃ thin films on miscut (001) SrTiO₃ substrates. *Appl. Phys. Lett.* **72**, 2963–2965 (1998).
47. Du, C. et al. Systematic variation of spin-orbit coupling with *d*-orbital filling: Large inverse spin Hall effect in 3*d* transition metals. *Phys. Rev. B* **90**, 140407 (2014).
48. Kresse, G. & Furthmüller, J. Efficient iterative schemes for ab initio total-energy calculations using a plane-wave basis set. *Phys. Rev. B* **54**, 11169–11186 (1996).
49. Perdew, Burke & Ernzerhof Generalized gradient approximation made simple. *Phys. Rev. Lett.* **77**, 3865–3868 (1996).
50. Pizzi, G. et al. Wannier90 as a community code: new features and applications. *J. Phys.: Condens. Matter* **32**, 165902 (2020).
51. Wu, Q. et al. WannierTools: an open-source software package for novel topological materials. *Comput. Phys. Commun.* **224**, 405–416 (2018).

Acknowledgements

The authors thank Dr. M. Kläui for the helpful discussions. This work is supported by the National Natural Science Foundation of China (Grant Nos. 62122008, 61971024, 11934016, 12274443, 12304149, 12074024, and 12174018); the Guangdong Basic and Applied Basic Research Foundation (Grant Nos. 2022A1515110648, 2023A1515010953); the National Key R&D Program of China (Grants Nos. 2022YFA1403302, 2022YFA1402600 and 2023YFA1406003); the Fundamental Research Funds for the Central Universities. J.R.S. is thankful for the support of the Science Center of the National Science Foundation of China (Grant No. 52088101), the Strategic Priority Research Program (B) of the Chinese Academy of Sciences (Grant No. XDB33030200) and the Project for Innovative Research Team of National Natural Science Foundation of China (Project No. 11921004).

Author contributions

Y.Z. planned and supervised the project. Y.Z. and F.R.H. conceived the idea and designed the experiments. F.R.H., Y.He, G.S.L., Y.Huang and H.Z. fabricated the devices. F.R.H., J.Z., B.L., Y.X.C., Q.S.J., J.E.Z, H.W.Y., and H.W. performed the measurements of the samples and analyzed the data. Q.H.Z. performed the STEM imaging. F.Y., H.Y.L., and X.-L.S. performed the density functional theory calculations. F.R.H., F.Y., and J.R.S. contributed to the theoretical explanation and data interpretation. F.R.H., J.S.C., W.S.Z., and Y.Z. cowrote the manuscript. All the authors read and commented on the manuscript.

Competing interests

The authors declare no competing interests.

Additional information

Supplementary information The online version contains supplementary material available at <https://doi.org/10.1038/s41467-024-51820-w>.

Correspondence and requests for materials should be addressed to Xian-Lei Sheng, Jirong Sun or Yue Zhang.

Peer review information *Nature Communications* thanks Purnima Balakrishnan and the other anonymous reviewer(s) for their contribution to the peer review of this work. A peer review file is available.

Reprints and permissions information is available at <http://www.nature.com/reprints>

Publisher's note Springer Nature remains neutral with regard to jurisdictional claims in published maps and institutional affiliations.

Open Access This article is licensed under a Creative Commons Attribution-NonCommercial-NoDerivatives 4.0 International License, which permits any non-commercial use, sharing, distribution and reproduction in any medium or format, as long as you give appropriate credit to the original author(s) and the source, provide a link to the Creative Commons licence, and indicate if you modified the licensed material. You do not have permission under this licence to share adapted material derived from this article or parts of it. The images or other third party material in this article are included in the article's Creative Commons licence, unless indicated otherwise in a credit line to the material. If material is not included in the article's Creative Commons licence and your intended use is not permitted by statutory regulation or exceeds the permitted use, you will need to obtain permission directly from the copyright holder. To view a copy of this licence, visit <http://creativecommons.org/licenses/by-nc-nd/4.0/>.

© The Author(s) 2024